

# Droplet morphology analysis of drop-on-demand inkjet printing

Hu-xiang Xia<sup>1</sup>, Takechi Kensuke<sup>2</sup>, Tajima Shin<sup>2</sup>, Kawamura Yoshiumi<sup>3</sup>, and \*Qing-yan Xu<sup>1</sup>

1. Key Laboratory for Advanced Materials Processing Technology (MOE), School of Materials Science and Engineering, Tsinghua University, Beijing 100084, China

2. Toyota Central R&D Labs., Inc., 41-1 Yokomichi Nagakute, Aichi 480-1192, Japan

3. Frontier Research Center, Toyota Motor Corporation, 1 Toyota-Cho, Toyota, Aichi 471-8572, Japan

Copyright © 2024 Foundry Journal Agency

**Abstract:** As an accurate 2D/3D fabrication tool, inkjet printing technology has great potential in preparation of micro electronic devices. The morphology of droplets produced by the inkjet printer has a great impact on the accuracy of deposition. In this study, the drop-on-demand (DoD) inkjet simulation model was established, and the accuracy of the simulation model was verified by corresponding experiments. The simulation result shows that the velocity of the droplet front and tail, as well as the time to disconnect from the nozzle is mainly affected by density ( $\rho$ ), viscosity ( $\mu$ ) and surface tension ( $\sigma$ ) of droplets. When the liquid filament is about to disconnect from the nozzle, the filament length and filament front velocity are found to have a linear correlation with  $\sigma/\rho\mu$  and  $\ln(\rho/(\mu\sigma^{1/2}))$ .

**Keywords:** microdevice fabrication; inkjet printing; droplet morphology; modeling and simulation

CLC numbers: TP391.9

Document code: A

Article ID: 1672-6421(2024)01-020-09

## 1 Introduction

Miniaturization has always been the trend in electronic equipment. Great achievements in the integration of microelectronic circuits and sensors make microelectronic devices widely used in today's life. In the context of device miniaturization, the demand for micro batteries continuously increases. To ensure the microelectronic devices can be effectively powered, it is necessary to further improve their energy and power density with their restricted size. While exploring high-capacity battery active materials, it is very important to develop fabrication technologies to effectively perform the materials' potential. Conventional electrode fabrication methods, such as electrochemical deposition<sup>[1-2]</sup>, chemical vapor deposition (CVD)<sup>[3-4]</sup>, physical vapor deposition (PVD)<sup>[5-6]</sup>, and atomic layer deposition (ALD)<sup>[7]</sup>, require cleanroom, expensive facilities and complex operation process, which restrict the manufacturing speed of small-sized energy source devices.

Inkjet printing, also known as droplet-based direct ink writing, is a high-efficient, cost-saving, non-impact 3D printing technology, which can precisely deposit 2D or 3D functional structures on various substrate. Many kinds of materials such as metals<sup>[8]</sup>, ceramics<sup>[9]</sup>, biomaterials<sup>[10]</sup>, or even 2D materials<sup>[11]</sup> can be used as the printing solute of the inkjet printers. These distinctive advantages making it widely and successfully applied in the flexible electronics<sup>[12-13]</sup>, life science<sup>[14-16]</sup>, and microelectronic energy source devices<sup>[17-20]</sup>. Inkjet printed materials obtain porous properties after sintering, and the pore size of materials can be artificially controlled by adjusting the size of nanoparticles in the ink and the subsequent sintering time, which is very suitable for the preparation of porous electrodes. Compared with the conventional electrode, the high porosity electrode printed by inkjet can increase the surface area of active material and lead to the high rate capacity.

To obtain the expected 3D microstructure, every single droplet needs to be deposited accurately, especially when printing a microelectrode array<sup>[21]</sup>. The influence of viscosity, surface tension and density on the droplet flying morphology should be very clear. The theory of pressure wave propagation proposed by Bogoy and Talke<sup>[22]</sup> is taken as the basis of printing condition analysis. This theory introduces the generation, motion and superposition rules of the pressure wave in the channel. In the study of ink properties, dimensionless

### \*Qing-yan Xu

Ph.D, Professor and doctoral supervisor. His research interests mainly focus on advanced casting forming, and multi-scale simulation research. He has presided over/participated in National Key R&D Programs, Major Projects of National Science and Technology, 973 projects, 863 projects, etc. To date, he has published more than 150 papers.

E-mail: scjxqy@tsinghua.edu.cn

Received: 2022-04-28; Accepted: 2022-08-11

criteria such as capillary number (Ca), Weber number (We), Ohnesorge number (Oh), and the reciprocal of the Oh number (Z), which indicate the relationships between the inertial force, viscous force and surface tension, are applied to predict the motion and morphology of droplets.

Jiang et al. [23] used one-dimensional simulation with MATLAB to predict the drop breakup, coalescence and meniscus movement of a drop-on-demand (DoD) inkjet. They proposed a rapid parametric analysis method for comprehensively analyzing nozzle dimension, driving pressure and fluid properties. Castrejón-Pita et al. [24] studied the thinning and breakup phenomenon of liquid filaments. Their experiment and simulation results show that thinning filament passes through a number of intermediate transient regimes, thereby delaying the onset of the inertial-viscous regime. This discovery has practical implications regarding the formation of undesirable satellite droplets. Xiao et al. [25] used Doppler vibration test with COMSOL to study the voltage wave, which provided a new idea for waveform design. Zhong et al. [26] proposed a non-dimensional number  $Pj = v \frac{dt}{D}$ , where  $v$ ,  $dt$  and  $D$  are droplet velocity, driving pulse and nozzle diameter, respectively, to analyze the droplet stability after ejection from an inkjet nozzle. In the second year, Wang et al. [27] from the same laboratory, studied the oscillation of the droplets and found that the deformation extent of droplet is strongly dependent on the Ca, it increases at first and then decreases as the Ca increases. Through many-body dissipative particle dynamics (MDPD), Suphanat et al. [28] discovered higher temperature and applied pressure can shorten droplet breakup time.

Previous researchers have made great efforts in theoretical research and engineering application of inkjet printing technology. In the research of inkjet, numerical simulation has gradually become an indispensable method to shorten the research cycle and obtain the information hard to get from experiments, such as pressure. The accuracy of numerical simulation can be guaranteed only with accurate inlet boundary condition. Due to the small size of the nozzle (~100 μm), it is nearly impossible to measure the extrusion velocity of the droplet at the nozzle through the experiments. Generally, in

the numerical simulation of inkjet, the velocity at the nozzle is considered to be constant during the injection. However, such simplification may lead to the decrease of simulation accuracy or even wrong results. In this study, based on the experimental results, a multistage velocity waveform was proposed to be the inlet boundary condition. The influence of each stage of velocity waveform on the droplet morphology and flight state was analyzed. Furthermore, the effect of ink properties including density, viscosity and surface tension under the multistage velocity waveform was studied.

## 2 Experimental description

Experiments were carried out with a DoD piezoelectric inkjet system, as shown in Fig. 1. A Labjet-600 (MICROJET Inc.) printer was used, which mainly contains a driving pulse controller, a pressure controller, a three axes platform system and a piezo-nozzle with an orifice radius of 40 μm. The pressure controller can keep the static pressure of the liquid in the reservoir at a proper level. The drive pulse controller provides various pulse waveforms to the lead zirconate titanate (PZT) piezo unit of the printer, as shown in Fig. 2(a). Under different voltage waveforms, PZT piezo unit produces different degrees of deformation, which precisely controls the expansion or reduction of the liquid channel. LED strobe, CCD camera and magnifier were combined to observe the morphology of the droplet. The CCD took pictures every 10 μs after giving the driving pulse. All the pictures taken by the CCD were enlarged until each pixel can be clearly seen. The displacement and morphological data of the droplet were recorded with a number of pixels. The effective pixels of the CCD were 768×494, and the size of the pixel in picture was 4.9 μm.

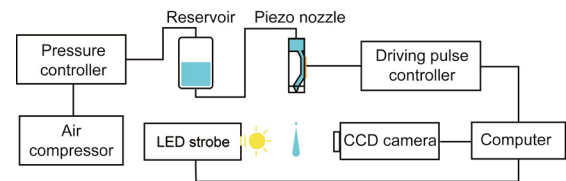


Fig. 1: Schematic diagram of the experimental system

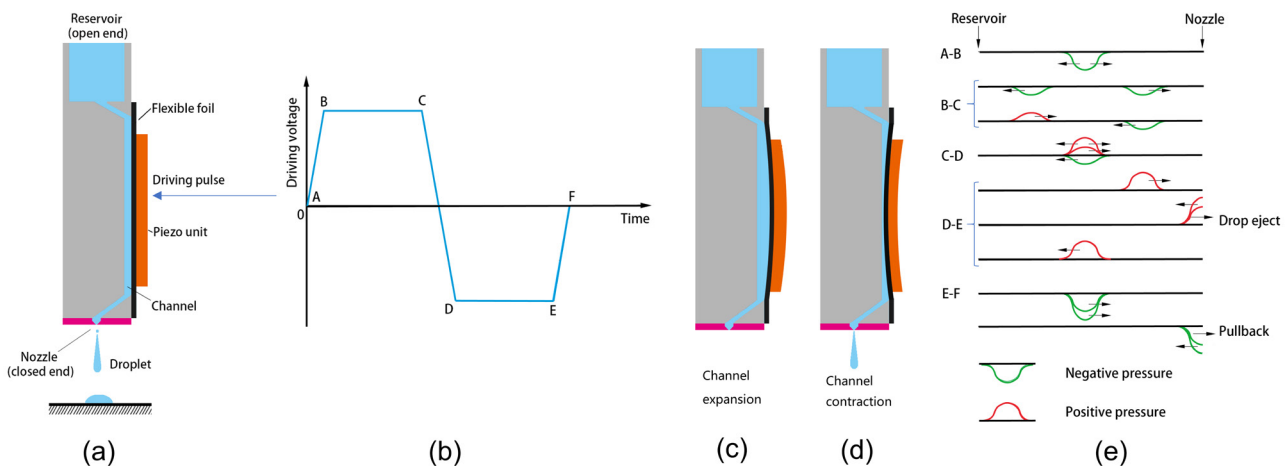


Fig. 2: Structure of piezo nozzle (a), driving waveform (b), schematic of channel expansion (c) and channel contraction (d), and pressure wave propagation in the channel (e)

The driving pulse determines the deformation of piezo unit and the propagation of the pressure wave in the liquid channel. Figure 2(b) shows the waveform of driving pulse in this experiment, which consists of five stages. In the first stage (A–B), the piezo unit deforms quickly under the action of the sharp rise of voltage, leading to a rapid expansion of the liquid channel, as shown in Fig. 2(c). The rapid expansion generates a negative pressure, then propagates along the channel to both ends, as described in Fig. 2(e). Under the positive voltage platform (B–C), the liquid channel keeps expanding. According to the reflection rules of acoustic waves, when the negative pressure wave moves to the nozzle (closed end) and the reservoir (open end), the original negative pressure wave will be converted into negative pressure wave and positive pressure wave, respectively with the same amplitude but the opposite propagation direction. The big voltage slope (C–D) makes the expanding channel contract, as shown in Fig. 2(d), and generates a positive pressure, which offsets the negative pressure propagating to the reservoir. The positive pressure generated in Stage C–D is superposed with the previous positive pressure and moves towards the nozzle under the negative voltage platform (D–E). When superposed positive pressure reaches the nozzle, the droplet ejects. In the last voltage slope (E–F), the liquid channel returns to its original shape, producing a negative pressure and finally causing a reverse pulling on liquid at the nozzle.

According to the pressure wave propagation theory, pressure resonance can be obtained by adjusting the pulse voltage width and interval<sup>[29]</sup>. However, due to the complexity and small size of the cavity structure in printer, the accurate waveform of pressure and velocity at the nozzle are difficult to describe at this stage. In the experiments, the dwell voltage ( $D_v$ ) and echo voltage ( $E_v$ ) are set to 65 V, the dwell time and echo time are set to 60  $\mu$ s.

Triethylene glycol monomethyl ether solution with Ag nanoparticles (Pvnanocell inc, 150TM-119) was used as printing ink. The average radius of the nanoparticles was about 80 nm. The density and surface tension of ink depend on the content of Ag. When the Ag content reaches 45wt.%, the density, surface tension and viscosity are 4.8 g·mL<sup>-1</sup>, 30 dyne·cm<sup>-1</sup>, and 34 cps (at 25 °C), respectively.

### 3 Mathematical model

Due to the low mass of the ink droplet, the effect of the air resistance on droplets cannot be ignored. The process of droplet generation and flying can be considered as a multiphase flow problem. The conservation of mass (continuity equation) and momentum equation (Navier-Stokes equation) were used to describe the flow of ink and air:

$$\frac{\partial \rho}{\partial t} + \nabla \cdot (\rho \vec{v}) = 0 \quad (1)$$

$$\frac{\partial}{\partial t} (\rho \vec{v}) + \nabla \cdot (\rho \vec{v} \vec{v}) = -\nabla p + \nabla \cdot (\vec{\tau}) + \rho \vec{g} + \vec{F}_{st} \quad (2)$$

where  $\rho$  is the density,  $\vec{v}$  is the axial velocity,  $p$  is the pressure,  $\vec{\tau}$  is the stress tensor,  $\rho \vec{g}$  and  $\vec{F}_{st}$  are the gravitational body

force and surface tension force. PISO algorithm (pressure implicit with splitting of operators)<sup>[30]</sup> was applied for solving this formula.

At the mesoscale, the effect of surface tension on droplet morphology is much greater than gravity. The continuum surface force (CSF) model<sup>[31]</sup> was used to calculate the surface tension, which interprets surface tension as a continuous effect across the interface, rather than as a boundary condition on the interface. The pressure drop across the surface can be represented as:

$$p_2 - p_1 = \sigma \left( \frac{1}{k_1} + \frac{1}{k_2} \right) \quad (3)$$

where  $p_1, p_2$  are the pressures of different phases on either side of the interface,  $\sigma$  is the tension coefficient (in units of force per unit length), and  $k_1, k_2$  are the surface curvature of different phases, which can be obtained by calculating the local gradient:

$$k = \nabla \cdot \hat{n} \quad (4)$$

where

$$\hat{n} = \frac{n}{|n|} \quad (5)$$

where  $n$  denotes the interface normal. The surface tension can be written in terms of the pressure jump across the surface. The force at the surface can be treated as a volume force, which can be expressed as following form:

$$\vec{F} = \sigma \frac{\alpha_1 \rho_1 k_2 \nabla a_2 + \alpha_2 \rho_2 k_1 \nabla a_1}{\frac{1}{2}(\rho_1 + \rho_2)} \quad (6)$$

where  $\alpha_i$  and  $\alpha_j$  are the volume fractions of the phase  $i$  and phase  $j$ .

VOF model<sup>[32]</sup> was used to track the interface between air and liquid. The nozzle inlet was set as velocity boundary condition, and the velocity profile can be expressed as following form:

$$v(r) = V_{cen} \left( 1 - \frac{r^2}{(cr_0)^2} \right) \quad (7)$$

where  $V_{cen}$  denotes the given velocity in the center of the parabolic profile,  $r$  is the distance to the center of the nozzle,  $r_0$  is the nozzle radius,  $c$  is defined as the velocity coefficient which related to the actual internal roughness of the nozzle and the ejecting velocity. In this work, by comparing the simulation results with the experimental results, it is found that when the value of  $\alpha$  is around 2.5, the simulation results are more consistent with the experiment results.

## 4 Results and discussion

### 4.1 Multi-stage velocity waveform analysis

Due to the rotational symmetry of the model, an axisymmetric 2D model with 210,207 grids was utilized. The average grid size was 2  $\mu$ m. The distance between the nozzle and the

substrate was set to 2 mm. The grid was refined at the region where the liquid flows through. Mesh-independent simulation was carried out to make sure the results were irrelevant to the mesh resolution. The zone between the inlet and the nozzle was filled with liquid, while the zone from the nozzle to the substrate was filled with air. The pressure at the outlet was set to 1 atm. The ink chamber and substrate were set as no-slip condition. Time step was 20 ns, and the continuity residual was less than  $10^{-8}$ .

The velocity waveform has a significant impact on simulation accuracy [25], while due to the diversity and complexity of cavity structure, it can hardly be deduced by mathematical methods. To obtain a velocity waveform consistent with the experimental results, a multi-stage velocity waveform was proposed, as shown in Fig. 3. In the multi-stage velocity waveform, C1 is a part of cosine function, C2 and C3 are two straight lines with different slopes, and C4 is also a straight line corresponding to the draw-back velocity.

The effect of each stage of multi-stage waveform on droplet

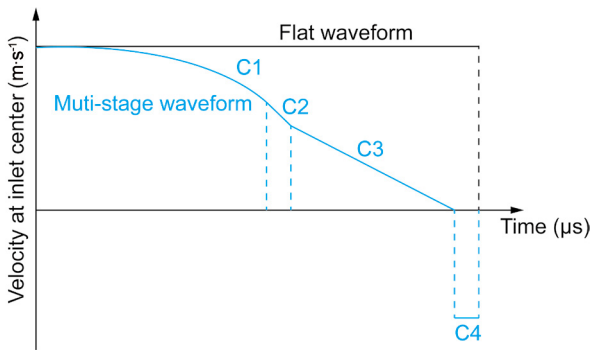


Fig. 3: Velocity waveform of nozzle

morphology is shown in Fig. 4. A certain stage in the velocity waveform can affect droplet morphology in many aspects, rather than one-to-one correspondence. The duration of C1 in the waveform is closely related to the breakup time which refers to the time when the main droplet separates from the filament. The longer the C1 lasts, the later the droplet breaks, and the larger the droplet radius is. The slope of C2 also has great influence on droplet breakup. With a smaller C2 slope, it takes a longer time for the liquid filament to break up from the nozzle, and the filament has a larger droplet radius. When the duration of C2 is over 5  $\mu\text{s}$ , increasing duration time has little effect on breakup velocity, breakup time and filament length. The draw-back velocity has a great influence on the maximum liquid column length [33]. Under a higher draw-back velocity, the nozzle generates a smaller curvature of the crescent, resulting in a higher necking position and a slower velocity at tail, which increases the filament length.

Figure 5 shows the experimental results (E) and the simulated results with multi-stage velocity waveform (S1) and flat velocity waveform (S2). The detail parameters of multi-stage velocity waveform are obtained from Fig. 4. The durations of C1, C2, C3, C4 of the multi-stage waveform are set to 40  $\mu\text{s}$ , 5  $\mu\text{s}$ , 75  $\mu\text{s}$ , 5  $\mu\text{s}$ , respectively. The slope of C2 and the draw-back velocity (C4) are set to 0.0234 and 1.2 times of the beginning velocity.

The inlet velocity waveform condition has great influence on the accuracy of simulation result. The morphology of the droplets under different waveforms is quite different, as shown in Figs. 5(a) and (b). The simulation result with multi-stage velocity waveform shows a much higher accuracy compared to the experimental result.

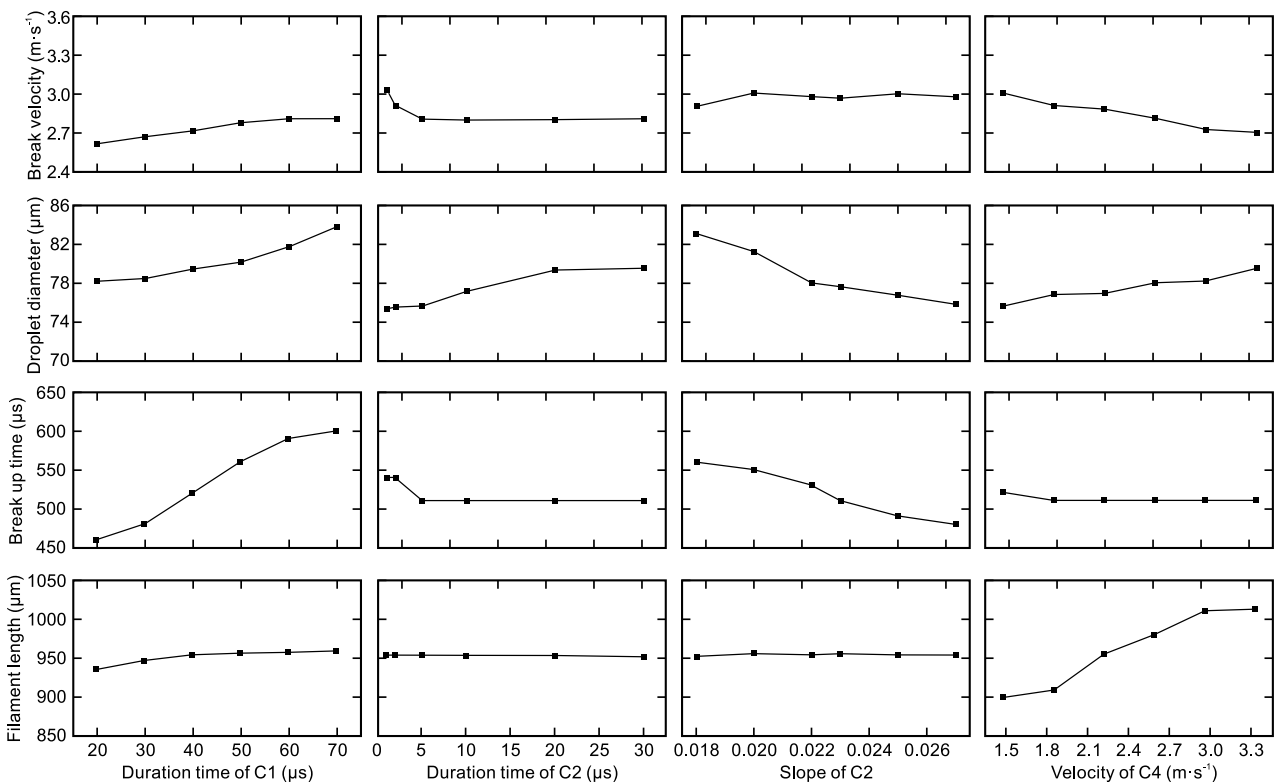
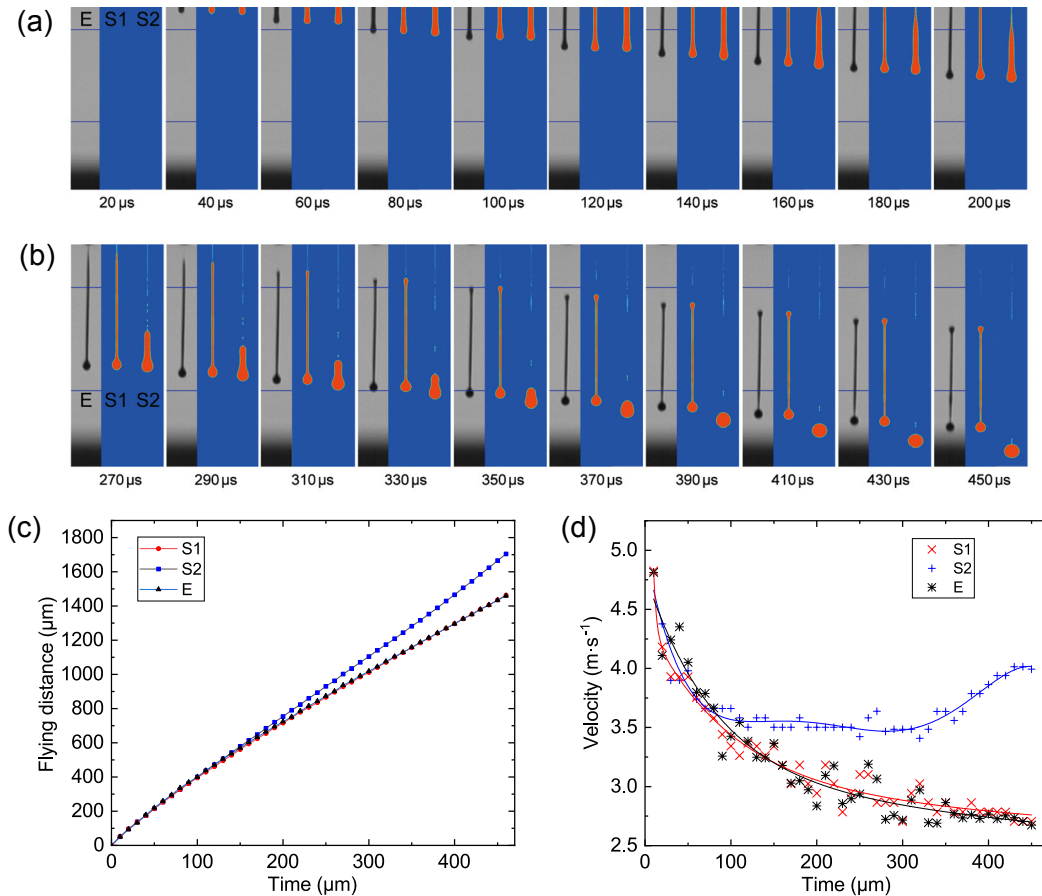


Fig. 4: Droplet morphology and injection status in each stage of multi-stage velocity waveform



**Fig. 5: Experimental results (E) and simulated results with multi-stage velocity waveform (S1) and flat velocity waveform (S2): (a) droplet generation process; (b) droplet flying process; (c) real time displacement; (d) real time velocity**

The analysis results of the real time displacement and velocity of the droplets are shown in Figs. 5(c) and (d). The simulated displacement under multi-stage velocity waveform is highly consistent with that of the experiment. At the beginning of ejection, the droplet velocity decreases sharply due to the surface tension and viscous force, as shown in Fig. 5(d). At this time, the filament with multi-stage velocity waveform still connects to the nozzle. The surface tension and viscous force at the nozzle are continuously dragging the droplet upward, reducing the velocity of the droplet. As the length of the filament becomes longer, the diameter of the liquid column at the nozzle decreases, as shown in Figs. 5(a) and (b). The dragging effect of surface tension and viscous force on the velocity keeps decreasing. As a result, the velocity at the front end of the droplet continuously decreases, but the decreasing rate is getting lower. In the case of flat waveform, because of the sudden decrease of velocity, filament disconnects from the nozzle soon after the injection. The velocity remains stable for a period of time, then the tail of the droplet accelerates to approach to the front end under the action of surface tension. Then, due to the impact of the tail to the front, the velocity of the droplet front begins to increase.

#### 4.2 Morphology analysis with different ink properties

The multi-stage velocity waveform was taken as the inlet boundary condition to study how the liquid properties affect

the droplet flight morphology. The influence of different densities on the droplet morphology is shown in Fig. 6. The front and tail of filaments at 340  $\mu\text{s}$  and 510  $\mu\text{s}$  are marked with green and black lines, respectively.

At the same flight time, for example, at 510  $\mu\text{s}$ , the tail of filaments with different densities is roughly kept at the same height. The velocity differences of filament tails are relatively small. In contrast, the height differences of filament fronts are obvious. With a higher density, the front of the filament flies farther and has higher velocity. This phenomenon can be explained by the effect of surface tension. The droplet with a lower density possesses smaller momentum. The limiting effect of surface tension is relatively obvious. The tail droplet is easy to merge with the head droplet to form a whole droplet. However, when the droplet has a higher density, it is difficult to form a single droplet due to its high momentum.

Figure 7(a) shows the filament length change during the flight process. At beginning, the length of liquid filament increases almost linearly. Then, as the filament disconnects from nozzle, the growth rate suddenly decreases. The end of the liquid filament spheroidize rapidly under the effect of surface tension, resulting in a rapid shortening of the liquid filament length. After the disconnection, the filament tail moves toward the filament front, and due to the velocity difference between filament front and tail, the filament length is in the state of increase, decrease or not change. In this case,

the disconnection times are approximately the same, which indicates that the ink density is not the main factor affecting droplet disconnection time from nozzle.

The radius change of the filament front is shown in Fig. 7(b). It increases linearly after the droplet ejecting from the nozzle. Then, after droplet disconnects from the nozzle, the radius growth rate slows down and finally tends to be fixed. There is no obvious oscillation of droplets under current printing parameters. Droplets with a higher density tend to have a lower radius and radius growth rate.

Viscous force is a kind of surface force that hinders the

irreversible deformation of a droplet. Figure 8 illustrates the influence of viscous force on the ejection process. Droplets with a low liquid viscosity are easily dispersed into multiple droplets. The high viscosity droplets have stronger adhesive force inside, which can better ensure the continuity of the liquid. As the viscosity increases, the droplet is subjected to a greater upward drag force during the ejection process, resulting in a decrease in the velocity of the droplet. To disconnect from the nozzle or breakup to form a main drop, droplet with a higher viscosity needs to overcome the greater viscosity force, which leads to the lower flying velocity and the longer disconnection time.

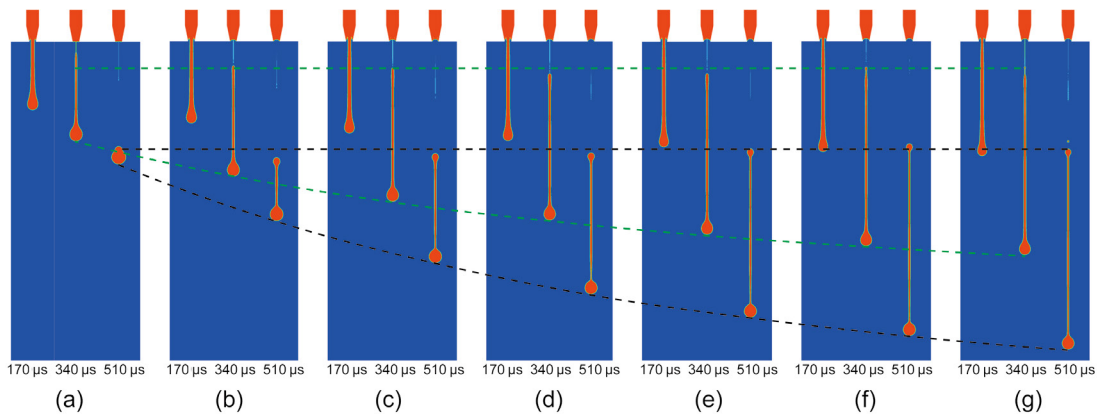


Fig. 6: Influence of density on droplet morphology: (a) 700 kg·m<sup>-3</sup>; (b) 1,000 kg·m<sup>-3</sup>; (c) 1,300 kg·m<sup>-3</sup>; (d) 1,600 kg·m<sup>-3</sup>; (e) 1,900 kg·m<sup>-3</sup>; (f) 2,200 kg·m<sup>-3</sup>; (g) 2,500 kg·m<sup>-3</sup>

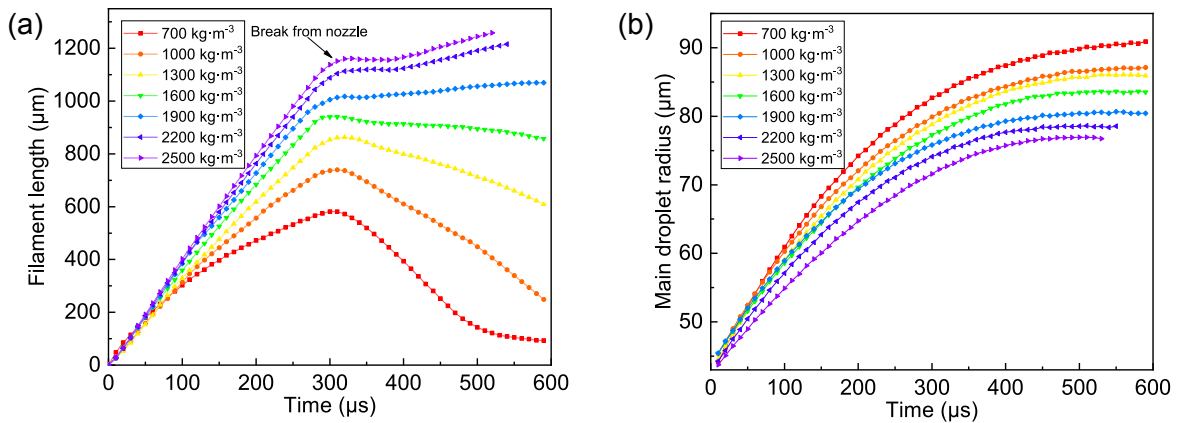


Fig. 7: Real-time changes of filament length (a) and main droplet radius (b) under different liquid densities

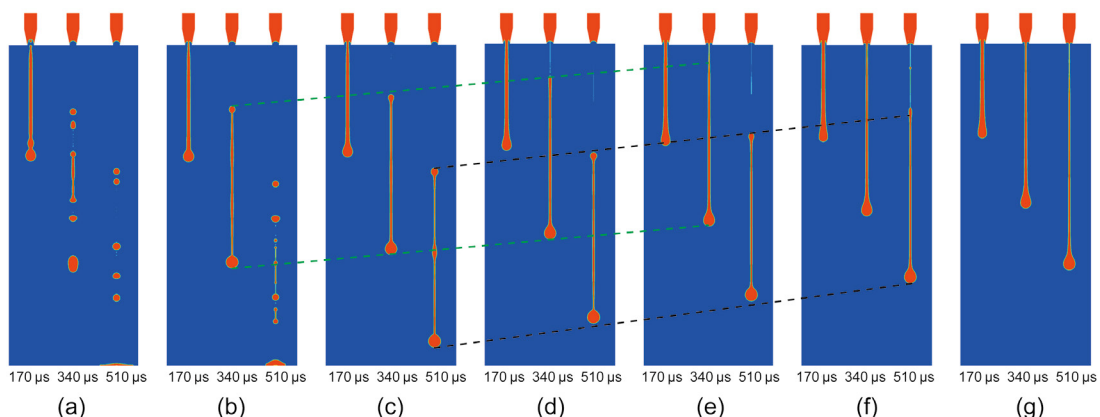


Fig. 8: Influence of viscosity on droplet morphology: (a) 1 cps; (b) 10 cps; (c) 20 cps; (d) 30 cps; (e) 40 cps; (f) 50 cps; (g) 60 cps

The filament length change is shown in Fig. 9(a). It should be noted that when the liquid filament breaks into two or more droplets, the filament length refers to the distance between the front of the first drop and the end of the last drop. In the observation area (from the nozzle to the substrate), although the droplet flying velocity and the disconnection time are different, the difference of filament length remains in a relatively small range. The variation trend of droplet radius, as shown in Fig. 9(b), is similar to the influence of density. After droplet injection, the radius increases linearly, then the growth rate decreases, and finally tend to be stable.

The effect of surface tension is shown in Fig. 10. Liquid droplets with high surface tension tend to reduce the surface area spontaneously because of their high surface energy. Droplets with high surface tension have greater internal forces and tend to form spheres. The filament with the higher surface tension possesses lower velocity at the front and the higher velocity at the tail. In the process of injection, the resultant force of the surface tension on the droplet is upward, so with bigger liquid surface tension, the droplet is subjected to greater upward resultant force, which reduces the velocity of droplet front. After the tail is necked, the resultant force of the surface tension at the droplet tail is downward. With the bigger liquid surface tension, the droplet is subjected to a greater downward resultant force, resulting in a higher downward velocity at the filament tail.

Under the same viscous force, droplet with the bigger surface tension possesses the greater driving force and tends to shrink into a sphere. Therefore, the droplet is more likely to disconnect from nozzle, and form shorter filament. Maximum filament length at  $70 \text{ dyn}\cdot\text{cm}^{-1}$  is  $597.5 \mu\text{m}$ , while the maximum filament length at  $10 \text{ dyn}\cdot\text{cm}^{-1}$  reaches  $1,774.5 \mu\text{m}$ , as shown in Fig. 11(a). The time when the droplet disconnects from the nozzle is obviously nonlinear with the surface tension. Droplets with a lower surface tension disconnect faster than those with a higher surface tension. The effect of surface tension on the disconnection time at the nozzle is also reflected in the radius change. As shown in Fig. 11(b), high surface tension droplets form stable main droplets much faster than low surface tension droplets.

From the above data and analysis, it is clear that, under the same multi-stage velocity waveform, the density, viscosity and surface tension all have obvious effects on droplet morphology. The time when the droplet disconnects from the nozzle is very critical. The filament length, droplet radius and velocity before and after the disconnection can be completely different. The filament length and filament front velocity at disconnection are found to have obvious linear correlation with  $\sigma/\rho\mu$  and  $\ln(\rho/(\mu\sigma^{\frac{1}{2}}))$ , as shown in Fig. 12. This linear relationship indicates that the density ( $\rho$ ), viscosity ( $\mu$ ), and surface tension ( $\sigma$ ) have a direct and obvious impact on liquid filament length and filament front velocity.

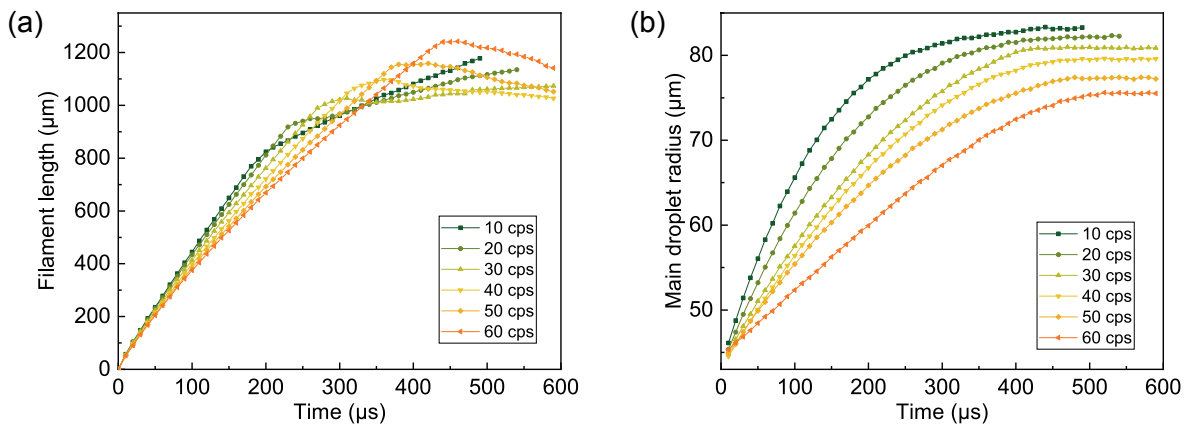


Fig. 9: Real-time changes of filament length (a) and main droplet radius (b) under different viscosities

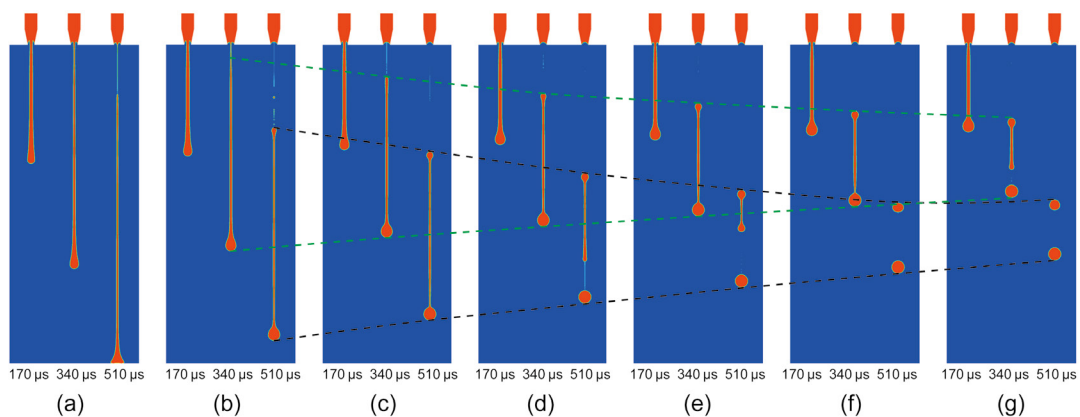


Fig. 10: Influence of surface tension on droplet morphology: (a)  $10 \text{ dyn}\cdot\text{cm}^{-1}$ ; (b)  $20 \text{ dyn}\cdot\text{cm}^{-1}$ ; (c)  $30 \text{ dyn}\cdot\text{cm}^{-1}$ ; (d)  $40 \text{ dyn}\cdot\text{cm}^{-1}$ ; (e)  $50 \text{ dyn}\cdot\text{cm}^{-1}$ ; (f)  $60 \text{ dyn}\cdot\text{cm}^{-1}$ ; (g)  $70 \text{ dyn}\cdot\text{cm}^{-1}$

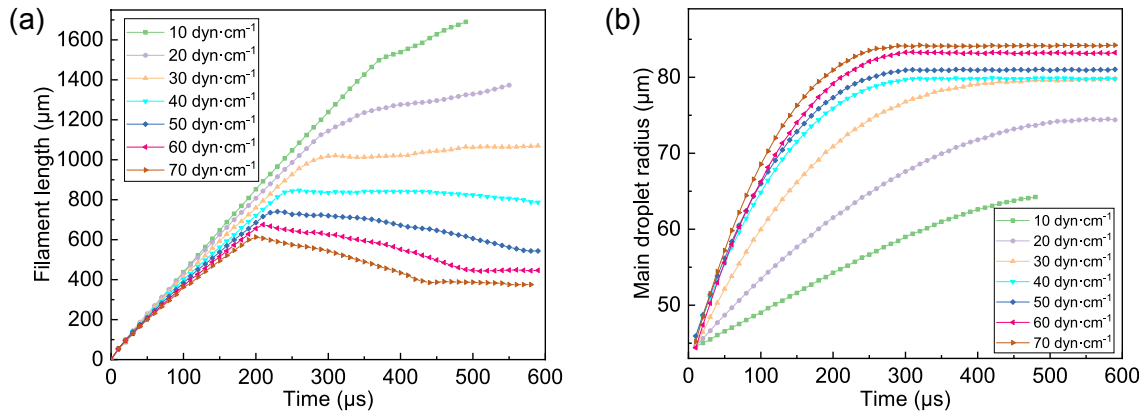


Fig. 11: Real-time changes of filament length (a) and main droplet radius (b) under different surface tension

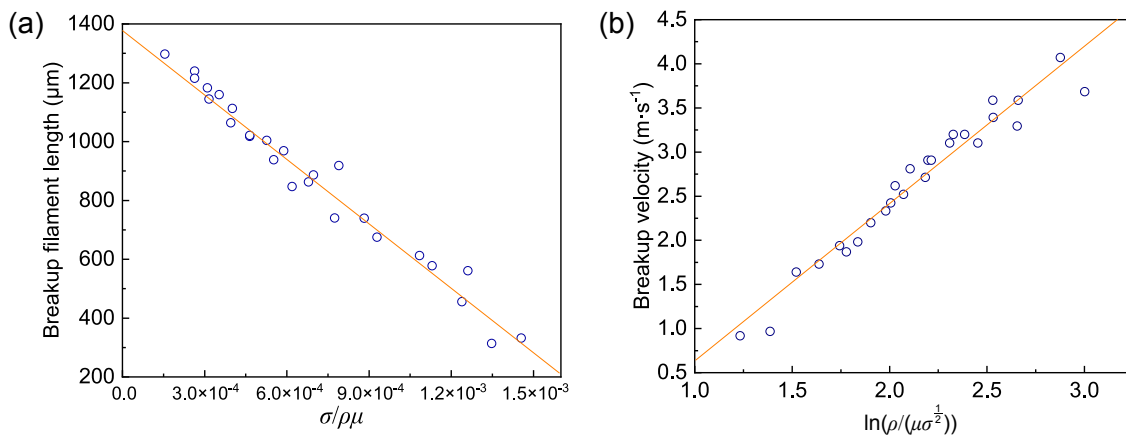


Fig. 12: When droplet is about to disconnect from the nozzle, the filament length (a) and velocity (b) are linearly related to  $\sigma/\rho\mu$  and  $\ln(\rho/(\mu\sigma^2))$

## 5 Conclusion

Inkjet technology is a commendable technology to build 2D/3D structure with various materials. In this study, a multi-stage velocity waveform was proposed as the input boundary condition in the simulation. The accuracy of the multi-stage velocity waveform was verified through experiments. The influences of ink properties including density, viscosity and surface tension on droplet morphology were studied. The result shows that the droplet with a lower density ( $\rho$ ), viscosity ( $\mu$ ) and higher surface tension ( $\sigma$ ) tends to have larger radius. As the viscosity increases, the liquid filament tends to possess a lower velocity, and needs a longer time to disconnect from the nozzle. Filament with a higher surface tension possesses a lower velocity at the front and a higher velocity at the tail, resulting in a smaller length of the filament. When the filament is about to disconnect from the nozzle, the filament length and filament front velocity are found to have an obvious linear correlation with  $\sigma/\rho\mu$  and  $\ln(\rho/(\mu\sigma^2))$ .

## Acknowledgment

This work was supported by the Tsinghua University – Toyota Research Center Project.

## Conflict of interest

Authors declare that they have no conflict of interest.

## References

- [1] Beidaghi M, Wang C. Micro-supercapacitors based on three dimensional interdigital polypyrrole/C-MEMS electrodes. *Electrochimica Acta*, 2011, 56(25): 9508–9514.
- [2] Kim I H, Kim J H, Lee Y H, et al. Synthesis and characterization of electrochemically prepared ruthenium oxide on carbon nanotube film substrate for supercapacitor applications. *Advanced Materials*, 2005, 152(11): A2170–A2178.
- [3] Yoo J J, Balakrishnan K, Huang J, et al. Ultrathin planar graphene supercapacitors. *Nano Letters*, 2011, 11(4): 1423–1427.
- [4] Yang P H, Mai W J. Flexible solid-state electrochemical supercapacitors. *Nano Energy*, 2014, 8: 274–290.
- [5] Dudney N J. Solid-state thin-film rechargeable batteries. *Materials Science & Engineering B*, 2005, 116(3): 245–249.
- [6] Bates J B, Dudney N J, Neudecker B, et al. Thin-film lithium and lithium-ion batteries. *Solid State Ionics*, 2000, 135(1–4): 33–45.
- [7] Guan C, Liu J L, Wang Y D, et al. Iron oxide-decorated carbon for supercapacitor anodes with ultrahigh energy density and outstanding cycling stability. *ACS Nano*, 2015, 9(5): 5198–5207.

- [8] Park M, Im J, Shin M, et al. Highly stretchable electric circuits from a composite material of silver nanoparticles and elastomeric fibres. *Nature Nanotechnology*, 2012, 7(12): 803–809.
- [9] Derby B. Inkjet printing ceramics: From drops to solid. *Journal of The European Ceramic Society*, 2011, 31(14): 2543–2550.
- [10] Tappa K, Jammalamadaka U. Novel biomaterials used in medical 3D printing techniques. *Journal of Functional Biomaterials*, 2018, 9(17). <https://doi.org/10.3390/jfb9010017>.
- [11] Carey T, Cacovich S, Divitini G, et al. Fully inkjet-printed two-dimensional material field-effect heterojunctions for wearable and textile electronics. *Nature Communications*, 2017, 8(1): 1202–1202.
- [12] Gao M, Li L, Song Y, et al. Inkjet printing wearable electronic devices. *Journal of Materials Chemistry C*, 2017, 5(12): 2971–2993.
- [13] Li D, Lai W, Zhang Y, et al. Printable transparent conductive films for flexible electronics. *Advanced Materials*, 2018, 30(10): 1704738.1.
- [14] Ashammakhi N, Hasan A, Kaarela O, et al. Advancing frontiers in bone bioprinting. *Advanced Healthcare Materials*, 2019, 8(7): 1801048. <https://doi.org/10.1002/adhm.201801048>.
- [15] Duan B. State-of-the-art review of 3D bioprinting for cardiovascular tissue engineering. *Annals of Biomedical Engineering*, 2017, 45(1): 195–209.
- [16] Ma Z, Li S, Wang H, et al. Advanced electronic skin devices for healthcare applications. *Journal of Materials Chemistry B*, 2019, 7(2): 173–197.
- [17] Zhang C J, McKeon L, Kremer M P, et al. Additive-free MXene inks and direct printing of micro-supercapacitors. *Nature communications*, 2019, 10(1): 1–9. <https://doi.org/10.1038/s41467-019-09398-1>.
- [18] Li J, Delekta S S, Zhang P, et al. Scalable fabrication and integration of graphene microsupercapacitors through full inkjet printing. *ACS Nano*, 2017, 11(8): 8249–8256.
- [19] Da Costa T H, Choi J W. Low-cost and customizable inkjet printing for microelectrodes fabrication. *Micro and Nano Systems Letters*, 2020, 8(1): 1–6. <https://doi.org/10.1186/s40486-020-0104-7>
- [20] Giannakou P, Tas M O, Borgne B L, et al. Water-transferred, inkjet-printed supercapacitors toward conformal and epidermal energy storage. *ACS Applied Materials & Interfaces*, 2020, 12(7): 8456–8465.
- [21] Ho C C, Murata K, Steingart D A, et al. A super ink jet printed zinc-silver 3D microbattery. *Journal of Micromechanics & Microengineering*, 2009, 19(9): 094013.
- [22] Bogy D B, Talke F E. Experimental and theoretical study of wave propagation phenomena in drop-on-demand ink jet devices. *IBM Journal of Research and Development*, 1984, 28(3): 314–321.
- [23] Jiang H C, Tan H. One dimensional simulation of droplet ejection of drop-on-demand inkjet. *ASME International Mechanical Engineering Congress & Exposition*, 2017. doi:10.1115/IMECE2017-71190.
- [24] Castrejonpita J R, Castrejonpita A A, Thete S, et al. Plethora of transitions during breakup of liquid filaments. In: *Proceedings of the National Academy of Sciences of the United States of America*, 2015, 112(15): 4582–4587.
- [25] Xiao X L, Wang X, Chen D, et al. A waveform design method for piezoelectric inkjet printhead with Doppler vibration test and numerical simulation. *Microelectronic Engineering*, 2018, 196(9): 13–19.
- [26] Zhong Y, Fang H, Ma Q, et al. Analysis of droplet stability after ejection from an inkjet nozzle. *Journal of Fluid Mechanics*, 2018, 845: 378–391.
- [27] Wang S, Zhong Y, Fang H, et al. Deformation characteristics of a single droplet driven by a piezoelectric nozzle of the drop-on-demand inkjet system. *Journal of Fluid Mechanics*, 2019: 634–645.
- [28] Suphanat A, Elisa Y M A, Yeo J, et al. Many-body dissipative particle dynamics simulations of nanodroplet formation in 3D nano-inkjet printing. *Modelling and Simulation in Materials Science and Engineering*, 2019, 27(5).
- [29] Kim B H, Kim S I, Lee J C, et al. Dynamic characteristics of a piezoelectric driven inkjet printhead fabricated using MEMS technology. *Sensors & Actuators: A Physical*, 2012, 173(1): 244–253.
- [30] Issa R I, Ahmadi-Befrui B, Beshay K R, et al. A solution of the implicitly discretized reacting flow equations by operator-splitting. *Journal of Computational Physics*, 1990, 90(1): 267. [https://doi.org/10.1016/0021-9991\(90\)90207-H](https://doi.org/10.1016/0021-9991(90)90207-H).
- [31] Brackbill J U, Kothe D B, and Zemach C. A continuum method for modeling surface tension. *Journal of Computational Physics*, 1992, 100: 335–354.
- [32] Hirt C W and Nichols B D. Volume of fluid (VOF) method for the dynamics of free boundaries. *Journal of Computational Physics*, 1981, 39: 201–225.
- [33] Sun C, Chu X, Yan S, et al. Influence of input signal on injection performance for needle driven piezoelectric micro-jet device. *Microsystem Technologies*, 2021, 27(5): 2009–2019.